NANO LETTERS

pubs.acs.org/NanoLett

Letter

Physics-Consistent Generative Hologram Design for Multifocal Femtosecond Laser Fabrication

Bowen Chen, Hao Wu,* Xiaoxu Rao, Wenji Yang, Zeye Li, Jincheng Ni, Jiawen Li, Dong Wu, Yanlei Hu, and Chaowei Wang*

Cite This: *Nano Lett.* 2026, 26, 15030−15038

Read Online

ACCESS | Metrics & More | Article Recommendations | Supporting Information

ABSTRACT: Multifocal phase holography offers a route to parallel femtosecond laser micro- and nanofabrication, but conventional weighted Gerchberg−Saxton (GSW) phase retrieval requires target-specific iterations and does not jointly optimize the optical quantities governing exposure quality. Here we introduce PhyFlow, a physics-consistent invertible flow model that generates phase-only multifocal holograms from target multifocal patterns in a single inverse pass. A multiscale invertible backbone learns target-to-phase correspondence, while differentiable Fourier optics constraints optimize diffraction efficiency, focal uniformity, and target-shape preservation. Across focal numbers and array scales, PhyFlow matches or surpasses GSW in energy concentration, focal balance, and shape fidelity while reducing per-hologram generation time by 98.8%. Optical-field measurements and femtosecond laser writing further show improved dot-area consistency, narrower line width distributions, and fewer nontarget written features. PhyFlow therefore connects rapid learned hologram generation with physically optimized fields and more uniform parallel fabrication.

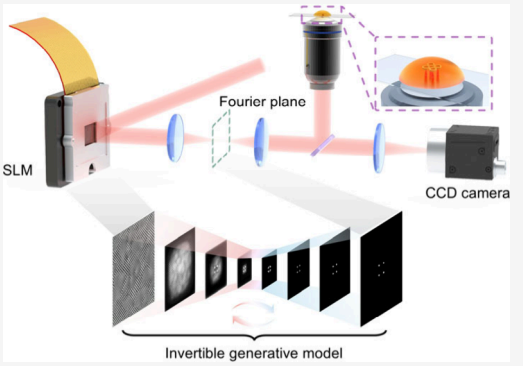

KEYWORDS: *femtosecond laser fabrication, spatial light modulation, computer-generated holography, multifocal phase holography, physics-consistent learning*

Computer-generated holography (CGH) enables programmable control of coherent light by numerically designing a wavefront that reconstructs a prescribed optical field after propagation. Combined with phase-only liquid-crystal-on-silicon spatial light modulators (LCoS-SLMs), CGH has become a versatile platform for micro- and nanostructure fabrication,[1−4] holographic display,[5−7] optical trapping,[8−10] and quantum photonics.[11−13] Multifocal phase holography is particularly attractive because it can redistribute a single incident beam into multiple addressable foci with controllable positions and intensities, thereby providing a general route to parallel optical manipulation, volumetric excitation, and high-throughput laser micro- and nanofabrication.[14−17]

In femtosecond laser direct writing, serial point-by-point exposure provides high three-dimensional resolution but intrinsically restricts fabrication throughput.[18,19] Parallel fabrication requires the incident beam to be divided into multiple writing foci that are generated simultaneously, positioned accurately, and supplied with comparable optical energy.[20−22] This requirement makes multifocal holography distinct from the reconstruction of a visually similar-intensity image. Each focus must deliver a controlled exposure dose, while residual nontarget light must remain sufficiently weak to avoid unintended polymerization. Unequal focal intensities lead to variations in feature size, whereas background response and system-dependent central leakage can expose the photoresist outside of the designed regions and generate unwanted structures. Therefore, hologram quality in multifocal femtosecond laser fabrication should be assessed using fabrication-relevant optical quantities, including diffraction efficiency, focal uniformity, target-shape fidelity, and suppression of nontarget response.[23,24] The central challenge is to satisfy these coupled requirements simultaneously rather than to optimize only the visual similarity of the reconstructed fields.

The Gerchberg−Saxton (GS) algorithm and its weighted variants remain standard tools for phase-only hologram design.[25] In multifocal holography, weighted GS-type methods (GSW) improve focal uniformity by iteratively reweighting target foci according to their reconstructed intensities, and adaptive weighting or artifact-suppression strategies can further enhance convergence and reconstruction quality.[26,27] These algorithms are physically interpretable and effective, but they are still target-specific phase-retrieval procedures: each new optical

Received: July 31, 2026
Revised: September 27, 2026
Accepted: October 5, 2026
Published: October 19, 2026

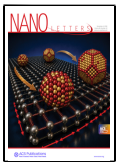

ACS Publications

© 2026 American Chemical Society

Downloaded from pubs.acs.org/naleld/article-pdf/26/43/15030/6890635/acs.nanolett.6c03779.pdf by UNIV SCIENCE AND TECHNOLOGY CHINA user on 07 November 2026

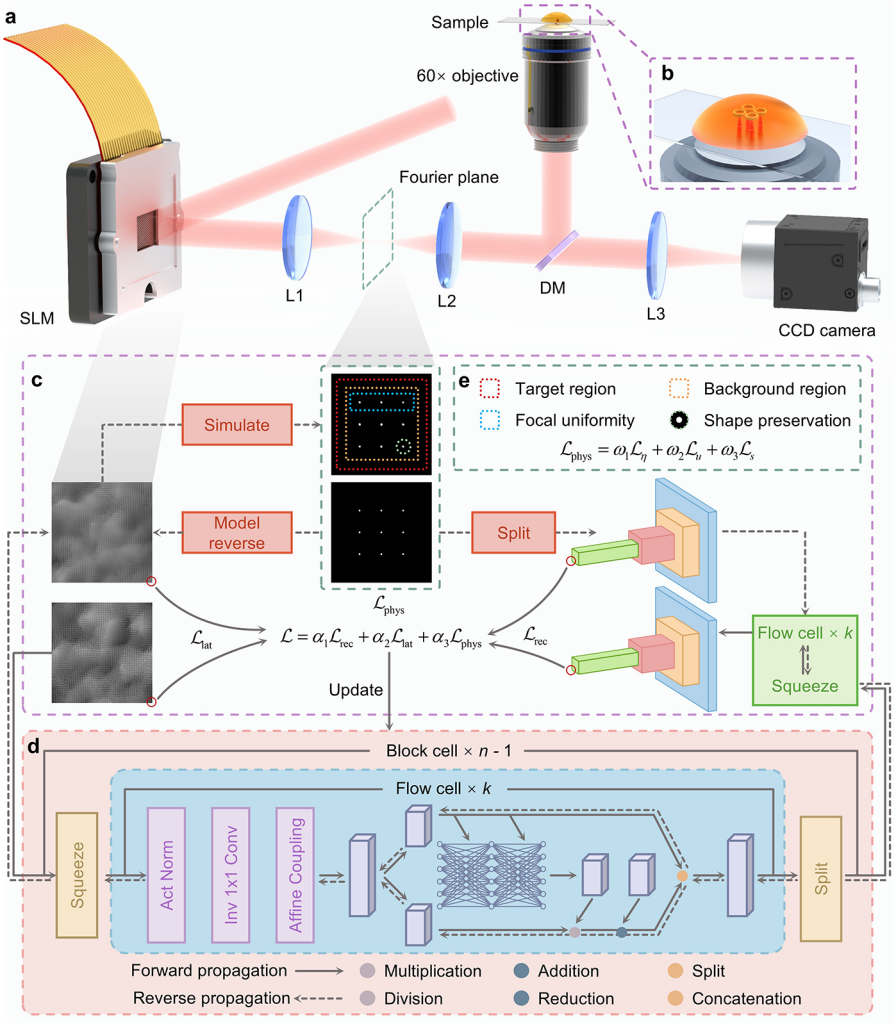

Figure 1. Optical system and PhyFlow framework. (a) Simplified optical path. (b) Magnified schematic of parallel two-photon polymerization in the photoresist. (c) Composite training objective of PhyFlow, including phase reconstruction, multiscale latent alignment, and physics consistency. (d) Glow-type invertible architecture used for bidirectional representation learning between target fields and phase holograms. (e) Schematic of the physics-consistency loss, which constrains diffraction efficiency, focal uniformity, and target-shape preservation in the propagated field.

field requires an independent iterative optimization. More importantly for fabrication-oriented holography, GSW updates primarily address focal equalization, whereas diffraction efficiency, target-shape preservation and nontarget response suppression are not explicitly coupled with focal balancing within a single propagation-domain objective. General nonconvex optimization frameworks can incorporate more flexible physical objectives for volumetric light shaping, lithography and neural photostimulation,[28,29] but they also rely on per-target numerical optimization. This iterative nature limits scalability for large-batch hologram generation, dynamic beam reconfiguration and real-time or adaptive fabrication workflows.

Learning-based CGH has shifted hologram synthesis from target-specific iterative optimization to trained inference.[30] DeepCGH and deep-learning-aided multifocal hologram generation have demonstrated that neural networks can substantially accelerate hologram calculation for volumetric and multifoci light-field generation.[31,32] However, these studies are primarily designed to reproduce target multifocal patterns, approximate iterative hologram solutions or predict optimization parameters. As a result, the optical quantities that directly determine parallel writing quality (energy concentration, focal dose balance, shape preservation, and nontarget response suppression) are often not placed at the center of the learning objective, and their influence on downstream femtosecond laser fabrication is rarely verified experimentally. Recent physics-driven neural holography has brought learned hologram generation closer to laser-processing applications. A three-dimensional coarse-to-fine holographic network incorporated vectorial diffraction and spherical-aberration modeling for millisecond-scale tight-focusing light-field modulation, with demonstrations in laser direct writing and fluorescence display.[33] SMART HoloTPL further embedded a broadband angular-spectrum polymerization model to enable speckle-free holographic two-photon lithography with high throughput and nanoscale resolution.[34] These studies demonstrate the value of embedding optical physics or material-response models into neural hologram generation. Nevertheless, multifocal parallel laser direct writing represents a different regime. Instead of reconstructing a continuous volumetric exposure pattern or suppressing speckle over an extended three-dimensional field, the hologram must generate discrete, spatially addressable focal arrays in which each focus delivers a comparable exposure dose while nontarget light remains below the polymerization

https://doi.org/10.1021/acs.nanolett.6c03779
Nano Lett. 2026, 26, 15030−15038

Downloaded from pubs.acs.org/naleld/article-pdf/26/43/15030/6890635/acs.nanolett.6c03779.pdf by UNIV SCIENCE AND TECHNOLOGY CHINA user on 07 November 2026

threshold. In this regime, small deviations in focal energy allocation or residual background response can be directly translated into dot-area variations, line width fluctuations and unintended written features. Moreover, most neural hologram generators treat hologram synthesis as a one-way mapping from a target field to a phase pattern, typically through feed-forward prediction or encoder−decoder inversion. Such formulations can accelerate computation but do not explicitly address the intrinsic nonuniqueness of phase-only holography, where multiple distinct phase distributions may produce similar target intensities. For multifocal fabrication, this ambiguity must be resolved while coordinating local phase textures with global energy allocation across the focal array. An invertible multiscale representation provides a suitable framework for this problem by preserving reversible image−latent mappings and learning cross-domain correspondence between target intensity fields and phase-only holograms. Therefore, a physics-consistent invertible framework that combines single-pass multifocal hologram generation, propagation-domain physical optimization and fabrication-oriented validation remains needed.

Here, we introduce PhyFlow, a physics-consistent invertible flow model for rapid multifocal phase hologram generation. PhyFlow learns a bidirectional multiscale representation between target multifocal patterns and phase-only holograms and generates a hologram through a single inverse pass. By coupling the invertible generator with differentiable Fourier optics propagation, the model is optimized not only for phase consistency with GSW-derived priors but also for diffraction efficiency, focal uniformity, and target-shape preservation in the propagated Fourier-plane field. We demonstrate that PhyFlow converts iterative hologram optimization into fast learned generation, reduces per-hologram generation time by 98.8% relative to GSW, and produces reconstructed fields that reach or exceed the GSW baseline in energy concentration, focal balance, and shape fidelity. Experimental optical-field measurements and femtosecond laser fabrication further demonstrate that these optical improvements translate into more uniform dot exposure, narrower line width distributions, and reduced nontarget written features. PhyFlow therefore provides a noniterative, physics-consistent route from learned multifocal hologram design to experimentally improved parallel femtosecond laser fabrication.

Figure 1 presents the optical configuration and the overall PhyFlow framework for rapid multifocal phase hologram generation and femtosecond fabrication. A phase-only hologram is displayed on the LCoS-SLM to modulate the incident femtosecond laser beam. The modulated wavefront is relayed through a 4f optical system and forms a programmable multifocal intensity distribution in the Fourier plane. The generated field is subsequently focused into the photoresist through a 60× oil-immersion objective to induce two-photon polymerization, while a CCD branch records the corresponding optical field for experimental validation (Figure 1a,b). The complete experimental optical path is shown in Figure S1. During training, normalized target multifocal patterns are paired with reference phase holograms generated by the GSW algorithm, providing data-driven phase priors for the model (see Supporting Information for details).

PhyFlow uses a Glow-type invertible flow as the core generative architecture (Figure 1d).[35] The network consists of stacked multiscale blocks, each composed of multiple flow steps. Each flow step contains ActNorm, an invertible convolution, and an affine coupling layer. Squeeze and split operations progressively reduce spatial resolution while increasing channel dimensionality, enabling the network to represent both local phase textures and global multifocal energy distribution patterns. This invertible formulation establishes a bidirectional representation between target light fields and phase holograms: the forward path maps images into a multiscale latent space, whereas the inverse path decodes target-field representations into phase-only holograms (see Supporting Information for details).

Unlike the original Glow model optimized by likelihood maximization, PhyFlow is trained to generate phase holograms that are both consistent with GSW-derived phase priors and physically effective after optical propagation. We therefore define a composite objective consisting of phase reconstruction, multiscale latent alignment and physics consistency (Figure 1c),

$$\mathcal{L} = \alpha_1 \mathcal{L}_{\mathrm{rec}} + \alpha_2 \mathcal{L}_{\mathrm{lat}} + \alpha_3 \mathcal{L}_{\mathrm{phys}} \tag{1}$$

where α_1, α_2, and α_3 balance the three terms. The phase reconstruction loss $\mathcal{L}_{\mathrm{rec}}$ constrains the generated hologram $\hat{\mathbf{H}}$ to remain close to the GSW reference $\mathbf{H}$,

$$\mathcal{L}_{\mathrm{rec}} = \|\hat{\mathbf{H}} - \mathbf{H}\|_1 \tag{2}$$

where $\|\cdot\|_1$ denotes the $\mathcal{L}_1$ distance, calculated throughout this work as the mean absolute difference over all elements of the corresponding tensors. Importantly, the GSW hologram is used here as a feasible phase prior rather than a unique ground-truth solution. Accordingly, $\mathcal{L}_{\mathrm{rec}}$ acts as a soft phase-level regularization term that stabilizes learning, while the latent-alignment and propagation-domain physics losses allow the generated phase to deviate from the reference when an alternative phase distribution yields an improved optical response. The latent-alignment loss encourages the target pattern $\mathbf{T}$ and the corresponding GSW hologram $\mathbf{H}$ to share consistent multiscale representations,

$$\mathcal{L}_{\mathrm{lat}} = \frac{1}{B} \sum_{b=1}^{B} \|\mathbf{z}_{\mathbf{T}}^{b} - \mathbf{z}_{\mathbf{H}}^{b}\|_1 \tag{3}$$

where B is the number of multiscale blocks in the model, $\mathbf{z}_{\mathbf{T}}^{b}$ and $\mathbf{z}_{\mathbf{H}}^{b}$ denote the latent variables encoded from $\mathbf{T}$ and $\mathbf{H}$ at the scale b, respectively. This term promotes cross-domain correspondence between the desired optical field and the phase pattern that generates it. To ensure that the generated phase is not only close to the reference hologram but also optically meaningful, we further introduce a differentiable Fourier-optics constraint.

The predicted phase was imposed on a unit-amplitude incident field to form the phase-modulated complex wavefront, which was then propagated to the Fourier plane using a centered two-dimensional Fourier transform. The resulting intensity distribution $\overline{I}(u,v)$ is peak-normalized before computing the physics-consistency loss $\mathcal{L}_{\mathrm{phys}}$, which is defined as

$$\mathcal{L}_{\mathrm{phys}} = \omega_1 \mathcal{L}_{\eta} + \omega_2 \mathcal{L}_{u} + \omega_3 \mathcal{L}_{s} \tag{4}$$

where ω_1, ω_2, and ω_3 balance the contributions of the three loss terms and $\mathcal{L}_{\eta}$, $\mathcal{L}_{u}$, and $\mathcal{L}_{s}$ correspond to diffraction efficiency, focal uniformity, and target-shape preservation, respectively (Figure 1e; see Supporting Information for details). The diffraction-efficiency term encourages optical energy to be concentrated inside the target region. The focal-uniformity term balances the mean intensities of different target components. The shape-preservation term constrains the normalized intensity distribution within the target mask, preventing the model from concentrating energy into a few isolated bright

https://doi.org/10.1021/acs.nanolett.6c03779
Nano Lett. 2026, 26, 15030−15038

Downloaded from pubs.acs.org/naleld/article-pdf/26/43/15030/6890635/acs.nanolett.6c03779.pdf by UNIV SCIENCE AND TECHNOLOGY CHINA user on 07 November 2026

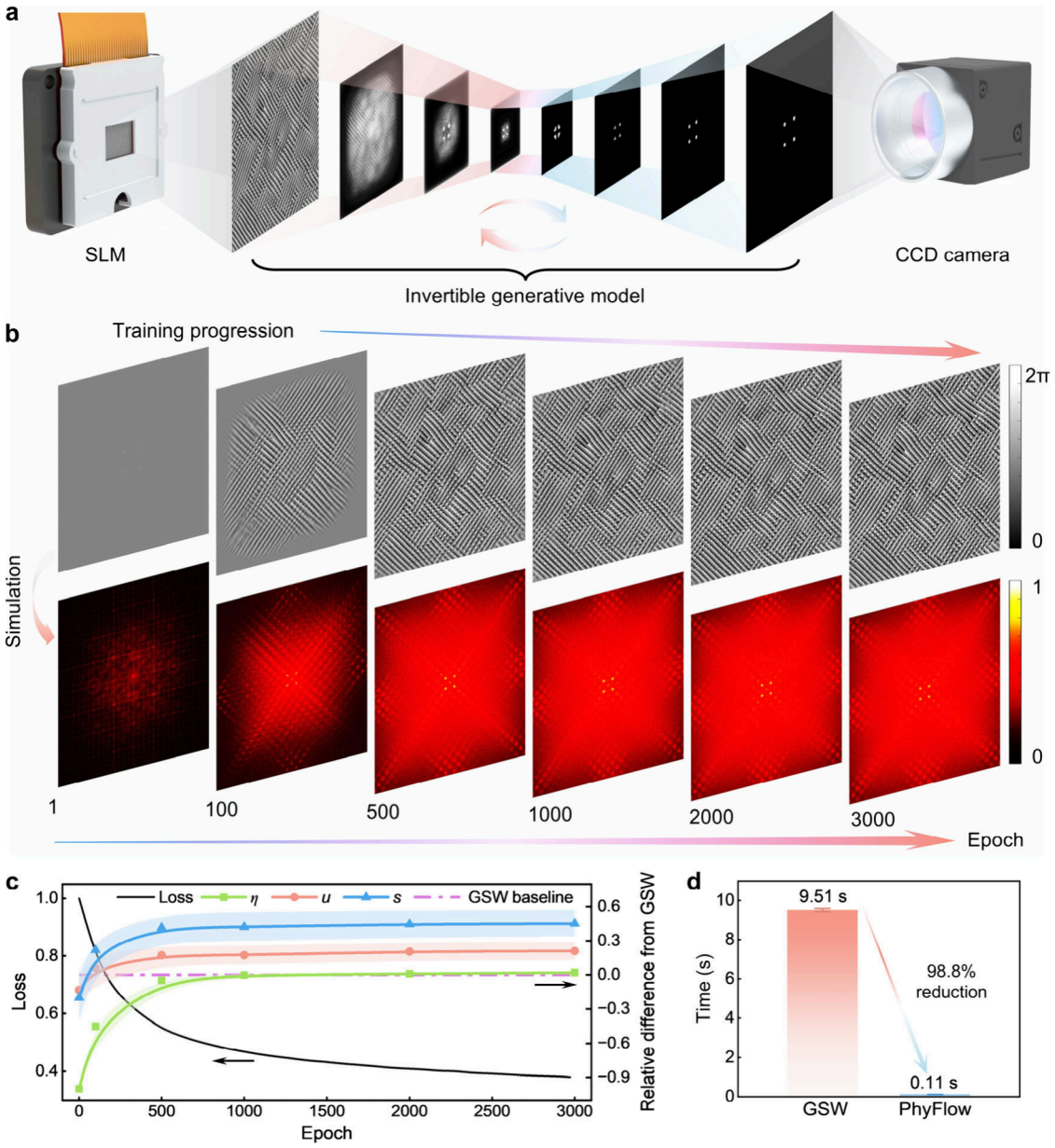

Figure 2. Training dynamics and evolution of optical-field metrics. (a) Invertible generation process. The target multifocal field and the GSW reference phase are mapped into a shared multiscale latent space, and the target latent representation is decoded through the inverse path to generate a phase-only hologram. (b) Evolution of generated phase holograms and corresponding simulated Fourier-plane fields during training. (c) Evolution of the total loss on the left *y*-axis and the relative physical metrics on the right *y*-axis. Diffraction efficiency, focal uniformity, and shape-preservation score are reported as relative differences from the corresponding GSW baselines. The curves show the mean values over eight test target patterns ($n = 8$) from a single training run. (d) Per-hologram generation time comparison between GSW and PhyFlow under the same timing protocol ($n = 400$).

pixels while neglecting the designed spot geometry. Together, these losses guide PhyFlow to generate phase holograms that preserve useful GSW phase priors while directly optimizing the propagated multifocal field.

Figure 2 summarizes the generative principle, training progression, and physical performance of PhyFlow. In contrast to GSW, which solves each target field by an independent iterative phase retrieval, PhyFlow learns the target-to-hologram mapping offline. Once trained, a target multifocal pattern can be converted to a phase-only hologram through a single inverse pass, thereby replacing per-sample optimization with amortized neural generation.

Figure 2a illustrates an invertible generative scheme. During training, the GSW reference phase **H** is encoded through the learnable invertible flow, whereas the target field **T** is decomposed by deterministic squeeze-and-split operations into a corresponding multiscale representation. The latent alignment loss brings these two representations into correspondence, after which the target-derived latent variables can be decoded through the inverse flow to generate a phase-only hologram. Owing to the invertibility of the flow architecture, the target latent representation can be decoded through the inverse path to obtain the generated phase hologram. This bidirectional formulation allows PhyFlow to organize hologram generation in a hierarchical latent space, where high-resolution latent variables retain local phase textures and fine spatial details, whereas low-resolution latent variables capture global array geometry and energy-allocation trends. The model therefore learns not only

https://doi.org/10.1021/acs.nanolett.6c03779
Nano Lett. 2026, 26, 15030−15038

Downloaded from pubs.acs.org/naleifd/article-pdf/26/43/15030/6890635/acs.nanolett.6c03779.pdf by UNIV SCIENCE AND TECHNOLOGY CHINA user on 07 November 2026

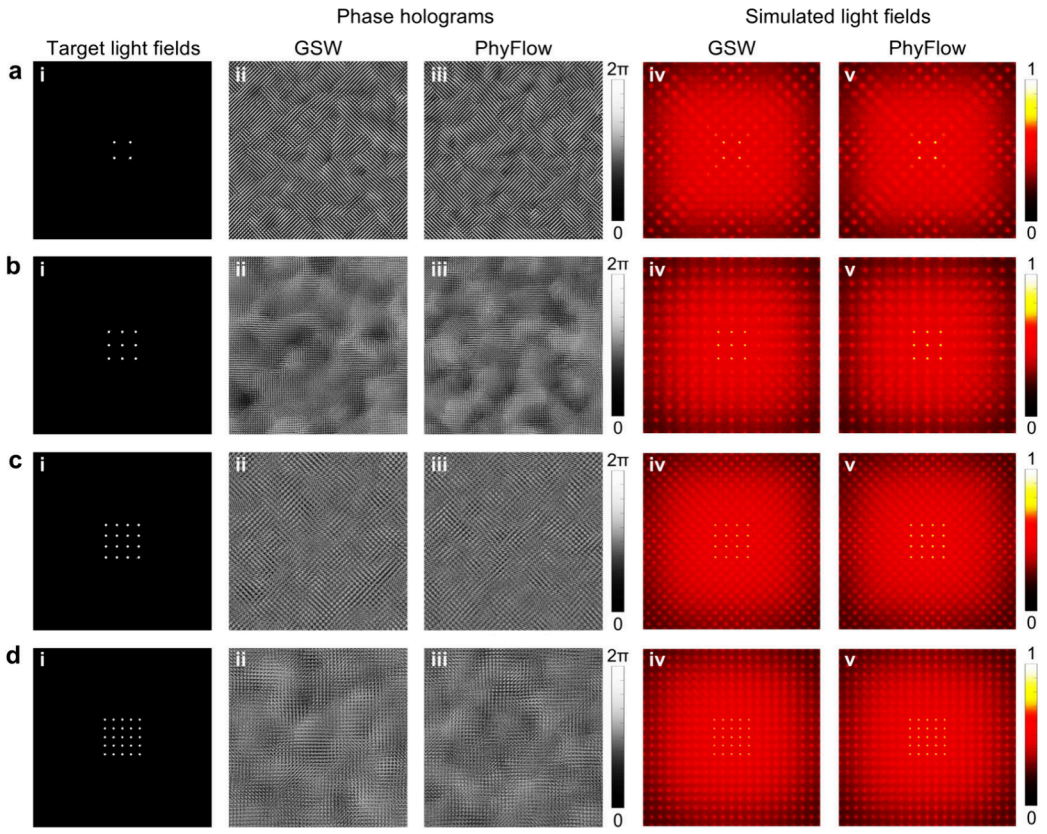

Figure 3. Simulated generalization across different multifocal arrays. (a–d) Representative multifocal targets with different focal numbers and array scales. Each row shows, from left to right, (i) target light field, (ii) GSW phase hologram, (iii) PhyFlow phase hologram, (iv) simulated Fourier-plane field generated by GSW hologram, and (v) simulated Fourier-plane field generated by PhyFlow hologram.

local phase modulation features but also global rules for redistributing optical energy across the multifocal field (detailed information is provided in Supporting Information).

The training evolution in Figure 2b reveals the progressive emergence of physically meaningful phase structures. The top row contains the generated phase patterns and the bottom row shows the corresponding simulated Fourier-plane fields. Unless otherwise stated, the simulated Fourier-plane fields shown in the figures are displayed after logarithmic dynamic-range compression to visualize both focal peaks and weak background structures; quantitative metrics were computed from uncompressed intensity distributions (see Supporting Information for details). At the initial stage, the generated phase lacks coherent high-frequency texture, and the propagated field contains weak target responses with pronounced speckles and energy leakage. As training proceeds, the phase evolves into spatially correlated textures, accompanied by increasingly localized foci, reduced background response, and improved interfocus balance. By the later epochs, the generated holograms produce stable multifocal reconstructions with suppressed central response, indicating that the learned inverse mapping has converged toward phase patterns that are both structurally organized and optically effective.

Figure 2c quantifies this evolution. The total loss decreases rapidly at early epochs and then approaches a stable regime. In parallel, the relative differences in diffraction efficiency η, focal uniformity u and shape-preservation score s all increase during training and ultimately approach positive values relative to the GSW baseline (see Supporting Information for details). Specifically, η improves by approximately 2%, indicating more efficient energy concentration within the target region, while u increases by approximately 21%, reflecting a more balanced energy distribution among foci. The largest gain is observed in s, which exceeds the GSW baseline by approximately 45%, showing that the normalized intensity profile within the target region more faithfully preserves the designed multifocal geometry. These results demonstrate that the physics-consistency loss drives the model beyond phase-image reconstruction toward improved optical-field performance.

Finally, Figure 2d compares the per-hologram generation times of GSW and PhyFlow under the same timing protocol. PhyFlow reduces the average generation time by approximately 86-fold (98.8% reduction) relative to GSW, converting an iterative phase-retrieval procedure into a single fast inverse generation step. Together, these results show that PhyFlow substantially accelerates multifocal hologram generation while maintaining, and in several metrics improving, the physical quality of the reconstructed optical field.

After confirming stable training dynamics and rapid non-iterative generation, we next examined whether the learned target-to-phase mapping generalizes across multifocal configurations with different focal numbers and array scales. During training, the phase reconstruction, multiscale latent alignment, and physics-consistency losses all decrease and converge to stable regimes (Figure S2), while the individual components of the physics loss exhibit consistent optimization trends (Figure S3). Ablation experiments further show that latent alignment improves the optical response, whereas the propagation-domain physical constraint provides additional gains in diffraction efficiency, focal uniformity, and target-shape preservation

https://doi.org/10.1021/acs.nanolett.6c03779
Nano Lett. 2026, 26, 15030−15038

Downloaded from pubs.acs.org/nalefd/article-pdf/26/43/15030/6890635/acs.nanolett.6c03779.pdf by UNIV SCIENCE AND TECHNOLOGY CHINA user on 07 November 2026

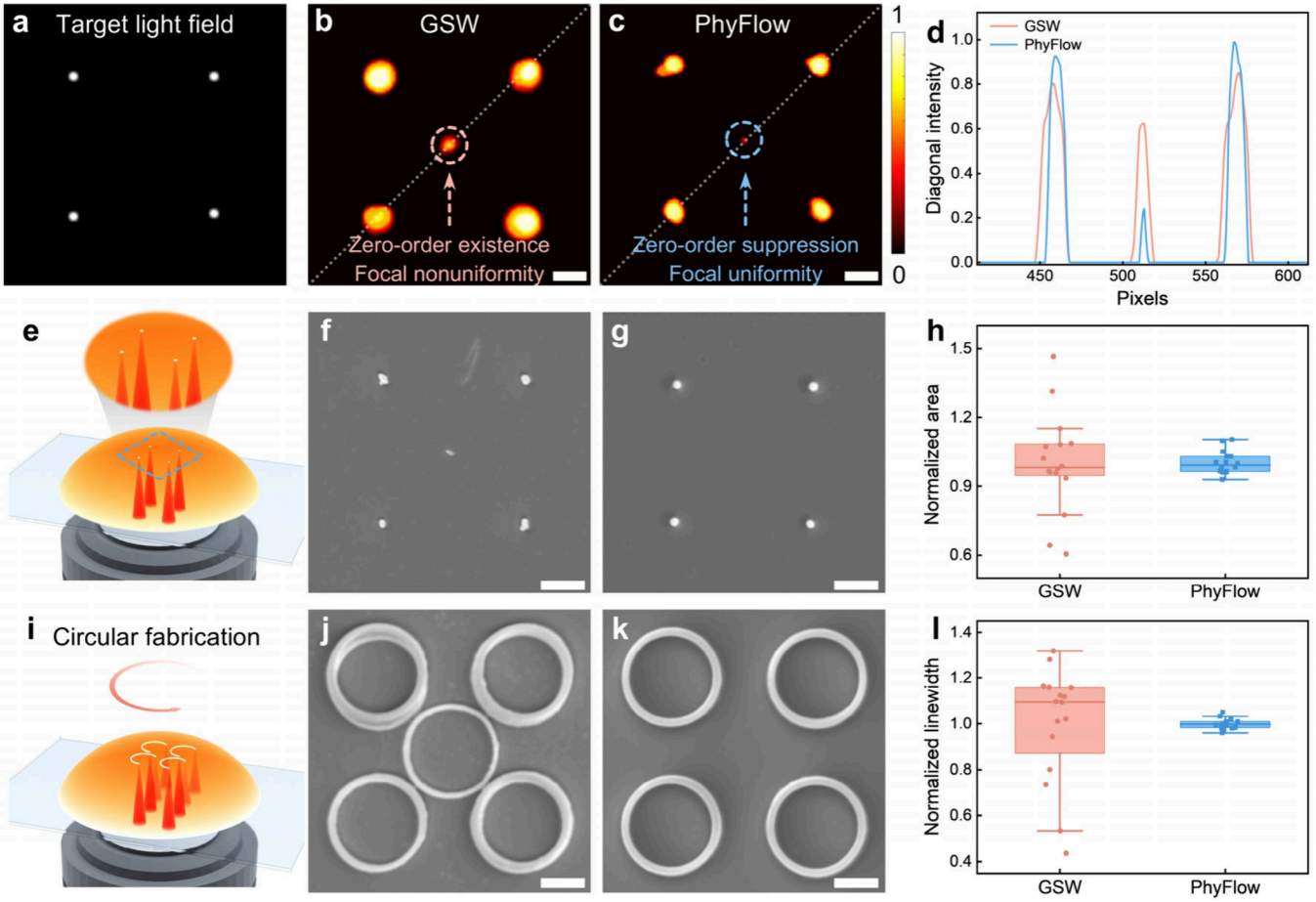

Figure 4. Experimental optical-field and femtosecond fabrication validation. (a) Ideal 2 × 2 target field. (b, c) CCD-recorded fields generated by the GSW and PhyFlow holograms, respectively. Scale bar, 5 μm. (d) Diagonal intensity profiles extracted along the dashed lines in parts b and c, crossing both target foci and the central residual-response region. (e) Schematic of single-exposure dot fabrication using a fixed multifocal field. (f, g) SEM images of dot arrays fabricated using the GSW and PhyFlow holograms, respectively. Scale bar, 5 μm. (h) Box plot of relative dot-area distributions (n = 4, data were collected from four independent fabrication experiments). (i) Schematic of circular scanning. (j, k) SEM images of circular trajectories fabricated using the GSW and PhyFlow holograms, respectively. Scale bar, 5 μm. (l) Box plot of relative line-width distributions for circular scanning (n = 4, data were collected from four independent fabrication experiments).

(Figure S4). These results indicate that the learned generator benefits from both GSW-derived phase supervision and propagation-domain physical optimization.

Figure 3 compares GSW and PhyFlow on representative multifocal targets selected from an independent test set that was not used during model training. Additional simulated reconstructions from the same independent test set, covering different focal numbers and spot sizes, are provided in Figure S5. The simulated Fourier-plane fields in Figure 3 are shown using the same log-compressed visualization protocol as in Figure 2b, and the corresponding peak-normalized linear-intensity fields are provided in Figure S6. For each target, PhyFlow generates a phase hologram whose local texture differs from the corresponding GSW solution, reflecting the nonunique nature of phase-only holography. Despite these differences in phase appearance, the simulated Fourier-plane fields accurately reproduce the prescribed focal positions and array geometry (see Supporting Information for details).

Across the tested configurations, the PhyFlow reconstructions show clearly resolved target foci, enhanced target-to-background contrast, and more faithful preservation of the designed spot patterns. In particular, the target foci show a higher apparent contrast under the same visualization protocol, while the surrounding background response is reduced relative to the target features. This behavior becomes especially important for denser arrays, where small errors in the energy allocation can blur individual foci or distort the intended geometry.

These results demonstrate that PhyFlow does not simply memorize or replicate the GSW phase textures. Instead, it learns a physically effective inverse mapping that can generate alternative phase solutions, producing high-quality multifocal fields after propagation. Therefore, the relevant criterion is not pixel-wise similarity to the GSW reference phase but the optical response of the generated hologram. The preservation of focal positions, target intensity, and array shape across different multifocal configurations supports the generalizability of PhyFlow for the rapid phase-only hologram generation. To further assess the applicability of the framework beyond the target distributions considered above, we additionally trained and evaluated PhyFlow on centered rectangular focal arrays and C-shaped target fields with varied geometric profiles (Figure S7). The corresponding simulations show that the same architecture and training strategy can accommodate both different focal array organizations and substantially different target field morphologies.

https://doi.org/10.1021/acs.nanolett.6c03779
Nano Lett. 2026, 26, 15030−15038

Downloaded from pubs.acs.org/naleld/article-pdf/26/43/15030/6890635/acs.nanolett.6c03779.pdf by UNIV SCIENCE AND TECHNOLOGY CHINA user on 07 November 2026

Having verified the simulated performance of PhyFlow, we next examined whether the learned holograms retain their optical advantages in the experimental system and whether these advantages translate into femtosecond laser direct writing. A 2 × 2 multifocal array was used as a representative target to establish the validation chain from optical-field generation to laser direct writing (Figure 4a). When the GSW and PhyFlow holograms were sequentially loaded onto the SLM under identical optical conditions, both methods produced four-focal patterns in the CCD plane (Figure 4b,c), confirming that the PhyFlow-generated phase can be directly implemented in the real optical system. Compared with GSW, the PhyFlow field exhibits more balanced focal intensities and a lower nontarget response near the field center, indicating improved energy redistribution in the experimentally generated multifocal field.

To quantify the optical field difference, we extracted diagonal intensity profiles from the recorded fields (Figure 4d). The selected profile passes through two target foci and the central region of the Fourier plane, thereby allowing simultaneous comparison of focal balance and residual nontarget intensity. The GSW profile shows a pronounced central response in addition to the two target-focal peaks, whereas the PhyFlow profile maintains comparable target-focal peaks with a 61.4% weaker central response (see Supporting Information for details). This reduction should be interpreted as an experimentally observed consequence of improved target-region energy concentration and nontarget background suppression.

We then evaluated whether the improved optical field leads to more consistent fabrication outcomes. In the single-exposure experiment, the fixed 2 × 2 multifocal field produced a dot array in the photoresist (Figure 4e). SEM characterization shows that both methods generated the designed four-dot pattern, but the GSW sample exhibits inconsistent dot size and an additional nontarget polymerized feature near the field center (Figure 4f). By contrast, the PhyFlow-fabricated dots are more uniform, and the nontarget central feature is strongly reduced (Figure 4g). Quantitative analysis of the relative dot area further confirms this trend (see Supporting Information for details). The GSW group exhibits a broader distribution, whereas the PhyFlow group is more tightly concentrated around unity (Figure 4h). Because dot area is directly related to local exposure dose, this result indicates more balanced energy delivery among the multiple writing foci.

Finally, we tested the continuous-path fabrication using circular scanning. In this mode, the multifocal field was kept optically fixed, while the piezoelectric nanopositioning stage translated the sample along prescribed circular trajectories to write multiple ringlike structures in parallel (Figure 4i). The GSW-generated field produced the target rings but also wrote an unintended trajectory associated with residual nontarget intensity during scanning (Figure 4j). In contrast, the PhyFlow-generated field produced the designed circular structures without a visible extra trajectory under the same exposure conditions (Figure 4k). The relative line width distribution is also narrower for PhyFlow than for GSW (Figure 4l), indicating more stable exposure during continuous scanning (see Supporting Information for details). Side-view SEM images of the circular structures and square-path scanning experiments further support this trend, showing cleaner and better-separated written features for PhyFlow than for GSW (Figure S8). Together, these results show that the optical-field improvements obtained by PhyFlow, including enhanced focal balance and reduced nontarget response, are reflected in the final material structures. The physics-consistent hologram-generation strategy therefore links propagation-domain optical optimization to improved uniformity and stability in multifocal femtosecond fabrication.

We have introduced PhyFlow, a physics-consistent invertible flow model for the rapid multifocal phase hologram generation. Unlike GSW algorithms, which optimize each target field through iterative phase retrieval, PhyFlow learns an invertible mapping between the target multifocal patterns and phase-only holograms. Once trained, the model generates holograms through a single inverse pass, converting target-specific iterative optimization to fast learned inference. By combining a GSW-derived phase prior, latent-space alignment, and a differentiable Fourier optics constraint, PhyFlow preserves useful structures from iterative phase retrieval while directly optimizing the propagated Fourier plane field for diffraction efficiency, focal uniformity, and target shape preservation.

During training, the generated phases progressively develop stable high-frequency textures, and the corresponding simulated fields show clearer target localization, improved focal uniformity, and reduced nontarget response. Quantitative analysis of diffraction efficiency, focal uniformity, and shape preservation demonstrates that the physics-consistency constraint extends the learning objective beyond phase-image similarity toward optical-field performance. Experimental optical field acquisition and femtosecond laser fabrication further confirm the practical value of PhyFlow. In the optical system, PhyFlow produces more uniform multifocal fields and a weaker residual central response than GSW under identical loading conditions. In single-exposure fabrication, this improvement is reflected by a more concentrated relative dot area distribution, indicating more uniform exposure delivery among the multiple foci. In circular scanning, PhyFlow yields narrower line width distributions and cleaner written trajectories than GSW. These results show that improvements in the propagated-field quality can be translated into measurable gains in multifocal fabrication consistency.

Overall, this study establishes a complete pathway from physics-consistent generative phase design to femtosecond-laser parallel fabrication. Future work may incorporate more accurate propagation models, system aberration calibration, and experimental feedback loops to improve the robustness in complex three-dimensional fields, multilayer exposures, and arbitrary scanning trajectories.

■ ASSOCIATED CONTENT

Data Availability Statement

The data that support the findings of this study are available from the corresponding authors upon reasonable request.

Supporting Information

The Supporting Information is available free of charge at https://pubs.acs.org/doi/10.1021/acs.nanolett.6c03779.

Supporting methods for multifocal and extended target-field data set construction, adaptive zero-order-suppressed GSW, PhyFlow architecture, Fourier optics propagation, physics-consistency loss, numerical metrics, model training, generation-time measurement, femtosecond-laser experiments, and quantitative image analysis; additional optical-path schematic, training and ablation analyses, simulated hologram reconstructions for multifocal, rectangular-array, and C-shaped targets, linear-intensity field comparisons, and SEM fabrication results (PDF)

Downloaded from pubs.acs.org/naleld/article-pdf/26/43/15030/6890635/acs.nanolett.6c03779.pdf by UNIV SCIENCE AND TECHNOLOGY CHINA user on 07 November 2026

https://doi.org/10.1021/acs.nanolett.6c03779
Nano Lett. 2026, 26, 15030−15038

AUTHOR INFORMATION

Corresponding Authors

Hao Wu − *School of Microelectronics, Hefei University of Technology, Hefei 230601, China; Department of Precision Machinery and Precision Instrumentation, University of Science and Technology of China, Hefei 230026, China;* orcid.org/0000-0003-4988-3900; Email: walech@hfut.edu.cn

Chaowei Wang − *Department of Precision Machinery and Precision Instrumentation, University of Science and Technology of China, Hefei 230026, China;* Email: chaoweiw@ustc.edu.cn

Authors

Bowen Chen − *School of Microelectronics, Hefei University of Technology, Hefei 230601, China; Department of Precision Machinery and Precision Instrumentation, University of Science and Technology of China, Hefei 230026, China*

Xiaoxu Rao − *Department of Precision Machinery and Precision Instrumentation, University of Science and Technology of China, Hefei 230026, China*

Wenji Yang − *Department of Precision Machinery and Precision Instrumentation, University of Science and Technology of China, Hefei 230026, China*

Zeye Li − *Department of Precision Machinery and Precision Instrumentation, University of Science and Technology of China, Hefei 230026, China*

Jincheng Ni − *Department of Precision Machinery and Precision Instrumentation, University of Science and Technology of China, Hefei 230026, China*

Jiawen Li − *Department of Precision Machinery and Precision Instrumentation, University of Science and Technology of China, Hefei 230026, China;* orcid.org/0000-0003-3950-6212

Dong Wu − *Department of Precision Machinery and Precision Instrumentation, University of Science and Technology of China, Hefei 230026, China;* orcid.org/0000-0003-0623-1515

Yanlei Hu − *Department of Precision Machinery and Precision Instrumentation, University of Science and Technology of China, Hefei 230026, China;* orcid.org/0000-0003-1964-0043

Complete contact information is available at: https://pubs.acs.org/10.1021/acs.nanolett.6c03779

Author Contributions

H. Wu, C. Wang, and B. Chen conceived the idea. B. Chen, X. Rao, W. Yang, Z. Li, and C. Wang performed the experiments and analyzed the results. B. Chen, W. Yang, and X. Rao prepared the manuscript. J. Ni, J. Li, D. Wu, Y. Hu, C. Wang, and H. Wu provided experimental equipment and assistance. All authors discussed the work and revised the manuscript.

Notes

The authors declare no competing financial interest.

ACKNOWLEDGMENTS

This work was supported by the National Key Research and Development Program of China (No. 2024YFB4610700), the National Natural Science Foundation of China (Nos. 62405307, 52375582, 62575274, 62325507, 62475252), CAS Project for Young Scientists in Basic Research (No. YSBR-049), the Fundamental Research Funds for the Central Universities (WK2090000088, WK2090250090), the National Science Foundation of Anhui (2408085MF151), and Joint Research Program of the Yangtze River Delta Community of Sci-tech Innovation (2024CSJGG00500).

REFERENCES

(1) Jiang, Z.; et al. De-coherent parallel laser processing of ultradense nanopores for high-density, large-area 3D optical phase encoding. *Nat. Commun.* **2026**, *17*, 1070.

(2) Asgari Sabet, R.; et al. Laser nanofabrication inside silicon with spatial beam modulation and anisotropic seeding. *Nat. Commun.* **2024**, *15*, 5786.

(3) Huang, L.; et al. Sub-wavelength patterned pulse laser lithography for efficient fabrication of large-area metasurfaces. *Nat. Commun.* **2022**, *13*, 5823.

(4) Yi, P.; et al. Reconfigurable holographic patterns for optical security multiplexing fabricated by 3D spatially modulated femtosecond pulses. *Light Adv. Manuf.* **2025**, *6*, 46.

(5) Li, S.-Q.; et al. Phase-only transmissive spatial light modulator based on tunable dielectric metasurface. *Science* **2019**, *364*, 1087−1090.

(6) Fan, X.; et al. Spatial light modulator via optically addressed metasurface. *Nat. Nanotechnol.* **2026**, *21*, 561−570.

(7) Dong, Z.; et al. Motion hologram: jointly optimized hologram generation and motion planning for photorealistic 3D displays via reinforcement learning. *Sci. Adv.* **2025**, *11*, No. eads9876.

(8) Chiou, P.; Ohta, A.; Wu, M. Massively parallel manipulation of single cells and microparticles using optical images. *Nature* **2005**, *436*, 370−372.

(9) Leite, I. T.; et al. Three-dimensional holographic optical manipulation through a high-numerical-aperture soft-glass multimode fibre. *Nat. Photonics* **2018**, *12*, 33−39.

(10) Kim, H.; et al. In situ single-atom array synthesis using dynamic holographic optical tweezers. *Nat. Commun.* **2016**, *7*, 13317.

(11) Sit, A.; et al. High-dimensional intracity quantum cryptography with structured photons. *Optica* **2017**, *4*, 1006−1010.

(12) Leach, J.; et al. Quantum correlations in optical angle−orbital angular momentum variables. *Science* **2010**, *329*, 662−665.

(13) Nape, I.; et al. Measuring dimensionality and purity of high-dimensional entangled states. *Nat. Commun.* **2021**, *12*, 5159.

(14) Liu, Y.; et al. Fabrication of functional micro−nano structures using phase holographically modulated femtosecond laser technology: a review. *Nanophotonics* **2025**, *14*, 3095−3114.

(15) Carstensen, M. S.; et al. Holographic resonant laser printing of metasurfaces using plasmonic template. *ACS Photonics* **2018**, *5*, 1665−1670.

(16) Zhang, Q.; et al. Light focusing and additive manufacturing through highly scattering media using upconversion nanoparticles. *Light Adv. Manuf.* **2025**, *6*, 248−259.

(17) Zhu, Y.; Nipu, S. M. A.; Chen, S.; Li, X. Linear volumetric additive manufacturing of polymer structures via light initiated direct growth. *Light Adv. Manuf.* **2025**, *6*, 710−723.

(18) Zhang, L.; et al. Functional shape-morphing microarchitectures fabricated by dynamic holographically shifted femtosecond multifoci. *Nano Lett.* **2022**, *22*, 5277−5286.

(19) Deubel, M.; et al. Direct laser writing of three-dimensional photonic-crystal templates for telecommunications. *Nat. Mater.* **2004**, *3*, 444−447.

(20) Zhang, L.; et al. High-throughput two-photon 3D printing enabled by holographic multi-foci high-speed scanning. *Nano Lett.* **2024**, *24*, 2671−2679.

(21) Gu, S.; et al. 3D nanolithography with metalens arrays and spatially adaptive illumination. *Nature* **2025**, *648*, 591−599.

(22) Obata, K.; Koch, J.; Hinze, U.; Chichkov, B. N. Multi-focus two-photon polymerization technique based on individually controlled phase modulation. *Opt. Express* **2010**, *18*, 17193−17200.

Downloaded from pubs.acs.org/naleld/article-pdf/26/43/15030/6890635/acs.nanolett.6c03779.pdf by UNIV SCIENCE AND TECHNOLOGY CHINA user on 07 November 2026

(23) Zhu, Y.; Zhao, W.; Zhang, C.; Wang, K.; Bai, J. Non-iterative multifold strip segmentation phase method for six-dimensional optical field modulation. *Opt. Lett.* **2022**, *47*, 1335−1338.
(24) Tian, W.; Zhu, L.; Xue, Z.; Wang, W.; Yu, J. Three-dimensional array optical tweezers based on array phase modulation. *Opt. Laser Technol.* **2025**, *184*, 112547.
(25) Gerchberg, R. W.; Saxton, W. O. A practical algorithm for the determination of phase from image and diffraction plane pictures. *Optik* **1972**, *35*, 237−246.
(26) Di Leonardo, R.; Ianni, F.; Ruocco, G. Computer generation of optimal holograms for optical trap arrays. *Opt. Express* **2007**, *15*, 1913−1922.
(27) Wu, Y.; et al. Adaptive weighted Gerchberg−Saxton algorithm for generation of phase-only hologram with artifacts suppression. *Opt. Express* **2021**, *29*, 1412−1427.
(28) Zhang, J.; Pégard, N.; Zhong, J.; Adesnik, H.; Waller, L. 3D computer-generated holography by non-convex optimization. *Optica* **2017**, *4*, 1306−1313.
(29) Sui, X.; He, Z.; Chu, D.; Cao, L. Non-convex optimization for inverse problem solving in computer-generated holography. *Light Sci. Appl.* **2024**, *13*, 158.
(30) Li, H.; et al. Redefinable neural network for structured light array. *Adv. Photonics Nexus* **2024**, *3*, 056015.
(31) Eybposh, M. H.; et al. DeepCGH: 3D computer-generated holography using deep learning. *Opt. Express* **2020**, *28*, 26636−26650.
(32) Qu, Z.; et al. Deep-learning-aided multi-focal hologram generation. *Opt. Laser Technol.* **2025**, *182*, 112056.
(33) Wu, J.; et al. Tight focusing holographic network enables 3D real-time and accurate light field modulation. *Laser Photonics Rev.* **2025**, *19*, 2401742.
(34) Liu, K.; et al. Model-driven deep learning enables speckle-free holography for 3D parallel nanofabrication. *Research* **2026**, *9*, 1159.
(35) Kingma, D. P.; Dhariwal, P. Glow: generative flow with invertible 1 × 1 convolutions. *Adv. Neural Inf. Process. Syst.* **2018**, *31*, 10215−10224.

Downloaded from pubs.acs.org/naleld/article-pdf/26/43/15030/6890635/acs.nanolett.6c03779.pdf by UNIV SCIENCE AND TECHNOLOGY CHINA user on 07 November 2026

https://doi.org/10.1021/acs.nanolett.6c03779
Nano Lett. 2026, 26, 15030−15038